

An elementary 158 km long quantum network connecting room temperature quantum memories

Dounan Du and Steven Sagona-Stophei

Department of Physics and Astronomy, Stony Brook University, Stony Brook, NY 11794, USA

Paul Stankus, Olli-Pentti Saira, and Dimitrios Katramatos

Brookhaven National Laboratory, Upton, NY, 11973, USA

Mael Flament and Mehdi Namazi

Qunnect Inc., 141 Flushing Av. Suite 1110, Brooklyn, NY, 11205, USA

Eden Figueroa

Department of Physics and Astronomy, Stony Brook University, Stony Brook, NY 11794, USA and Brookhaven National Laboratory, Upton, NY, 11973, USA

First-generation long-distance quantum repeater networks require quantum memories capable of interfacing with telecom photons to perform quantum-interference-mediated entanglement generation operations. The ability to demonstrate these interconnections using real-life fiber connections in a long-distance setting is paramount to realize a scalable quantum internet. Here we address these significant challenges by observing Hong-Ou-Mandel (HOM) interference between indistinguishable telecom photons produced in two independent room temperature quantum memories, separated by a distance of 158 km. We obtained interference visibilities after long-distance propagation of $V = (38 \pm 2)\%$ for single-photon level experimental inputs. This first-of-its-kind quantum network prototype connecting quantum laboratories in Stony Brook University and Brookhaven National Laboratory is envisioned to evolve into a large-scale memory-assisted entanglement distribution quantum network, the basis for inter-city quantum communication.

I. INTRODUCTION

Quantum information technologies, in which quantum mechanics' physical laws govern the control and transmission of information, show significant promise for revolutionary new capabilities that are fundamentally different from what is possible with classical technology alone [1]. Any quantum processing that takes place across multiple locations will require the preservation, transport, and sharing of quantum states across significant distances. Thus a widespread *quantum network* can usher in a new age of quantum information processing, with never-before-seen capabilities in communication, sensing, and computing [2]. Prime examples of such quantum network protocols are Measurement-Device-Independent Quantum Key Distribution (MDI-QKD) [3], and entanglement distribution using quantum repeaters [4].

Over the last decade, the experimental development of such networks' components has been widely pursued. Prototypes have demonstrated elementary quantum functionality, such as direct entanglement distribution [5–8], quantum-state transfer [9, 10], and short-distance interference-mediated entanglement generation between light-matter quantum nodes [11]. As we move forward in implementing large quantum networks, we can list a set of general properties that we would want to have to build an extended network to be practical [12]. These follow the discussions presented, for example, in the DOE-ASCR workshop “Quantum Networks for Open Science” [13], the NSF “Quantum Inter-Connects (QuICs) for Next-Generation Information Technologies” [14] and the DOE “Quantum Internet Blueprint Workshop” [15].

- **Portability.** The essential components of each node, particularly quantum memories and frequency converters, should all be portable, meaning that they can be manufactured centrally and then deployed in the field with minimal installation complexity.
- **Room temperature operation.** It will be of great advantage in any system to be built across a wide area and utilize a wide variety of locations to minimize environmental demands by the equipment. In particular, if all the components can work at room temperature without the need for cryogenic partitions or consumables.
- **Agnostic/signal independence.** Just as the operation of a digital data network is essentially independent of what data is being carried over it, the quantum network should have the capability to transport different kinds of quantum states. Such a network is termed *agnostic*, e.g. not fixed to any one specific computational basis.
- **Transparent.** The quantum network will also be greatly simplified if it is *transparent*, i.e. all-optical, with no optical-to-electrical-to-optical conversions across which it would be difficult to maintain entanglement at room temperature.
- **Compatible with telecom infrastructure.** The building of a quantum network will be greatly advanced if it can take advantage of the physical channels, particularly optical fibers, that have already been highly developed and widely deployed for data networks. In the case of using entangled photon pairs, this will require a photon-photon transduction capability between the wavelengths used by the sources, the memories, and existing telecom industry fiber channels.

One of the most promising avenues to build first-generation quantum networks is the use of atomic-ensemble-based optical quantum memories. These systems have recently shown to operate with high-efficiency [16] and long storage times [17]. Furthermore, elementary demonstrations of small quantum networks have also been performed recently [18, 19]. This work has focused on implementing the DLCZ protocol [20], by using Class 1 memories, which emit one photon first and another photon later on-demand, relying on quantum interference to generate entanglement [21]. Room-temperature quantum technology offers a very exciting solution to build these Class 1 memory-based quantum repeater networks [22]. Recent studies have demonstrated the potential of room-temperature quantum devices for this purpose, including the demonstration of noiseless room-temperature quantum memories for single-photons and polarization qubits [23–25] with coherence times of several seconds in ambient conditions [26]. Furthermore, preliminary quantum networks using room-temperature memories are already available [27, 28].

Here, we demonstrate the implementation of Class 1 room-temperature long-distance quantum network of two quantum light-matter interfaces and benchmark the inter-connectivity between its components at telecom wavelengths. We interconnected the quantum devices in a configuration akin to the one needed to perform the Cabrillo entanglement scheme [21]. This configuration requires two sources of telecom qubits (herein called Alice and Bob) generating single-photon level pulses. We have chosen Alice and Bob to be two room-temperature quantum memories performing transduction between the 795 and 1324 nm wavelengths [29]. After transmission in long-distance fiber links, the qubits are sent to the measurement station, where we investigate the indistinguishability of the two single-photon wave-packets produced in the memory using Hong-Ou-Mandel (HOM) interference [30]. We measure the two-detector coincidence rate as a function of the relative arrival time between the qubits.

We characterize our elementary long-distance quantum network in two different configurations. First, we show Mach-Zender interferometry of the memory-produced qubits in an interferometer with two 70 km long arms. Next, we demonstrate the degree of indistinguishability of the telecom polarization qubits transduced in two independent quantum memories using HOM interference experiments, with one arm of the interferometer being 70 km, and the second one being 88km, in order to achieve phase independency between the qubits.

II. TELECOM COMPATIBLE QUANTUM MEMORIES

The first step in our procedure is to demonstrate that our rubidium vapor quantum memory platform is compatible with telecom operation. This desired property has been demonstrated in proof of principle experiments with cryogenically cooled crystals [31–33], but not yet at room temperature.

A. Two-photon absorption and telecom laser rubidium stabilization

Stabilization of a 1367 nm diode laser to the rubidium transitions is achieved in the following manner. We apply an optical-optical double resonance (OODR) scheme to obtain the ^{85}Rb spectrum in the vicinity of $1.3\mu\text{m}$. Figure 2a shows the energy scheme. The $5\text{S}_{1/2} \rightarrow 5\text{P}_{3/2}$ transition($|1\rangle \rightarrow |3\rangle$) is 780nm and the $5\text{P}_{3/2} \rightarrow 6\text{S}_{1/2}$ $|3\rangle \rightarrow |4\rangle$ is 1367nm. A 780nm pump laser is used to increase the population in the $5\text{P}_{3/2}$ level. The pump laser is locked to the $5\text{S}_{1/2}\text{F} = 3 \rightarrow 5\text{P}_{3/2}\text{F}' = 4$ transition via a Doppler-free saturated absorption spectroscopy (SAS) system. The 1367nm laser is conterpropagating with the pump laser beam in a 7cm long Rubidium reference cell. The cell is maintained at 60°C . A InGaAs balanced amplified photodetector is used to obtain the spectrum signal. We scan the 1367nm laser while keeping the pump laser locked to obtain the OODR spectrum. We generate the error signal by modulating the 1367nm laser at 100kHz and use a standard locking loop, as shown in Figure 1.

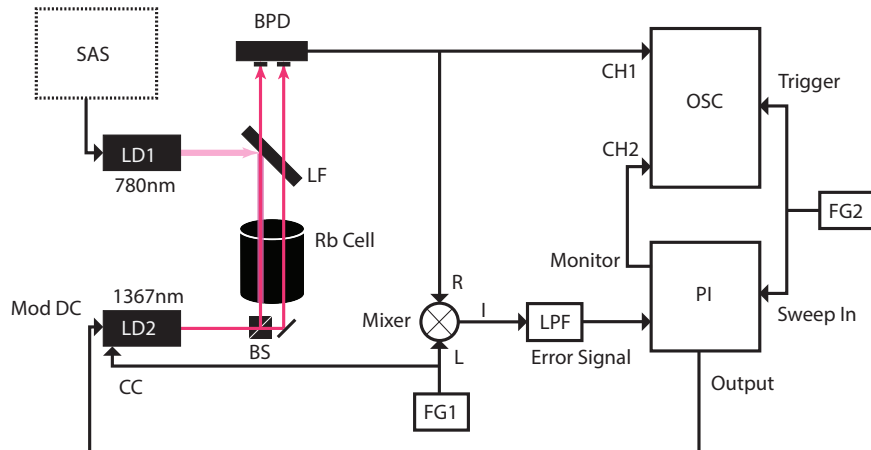


FIG. 1. The laser stabilization setup. SAS: saturated absorption spectroscopy setup; LD: laser diode; BS: beam splitter; LF: long pass filter; BPD: balanced amplified photodetector; FG1: function generator generating 100kHz laser current modulation signal; FG2: function generator used to generate 10Hz signal for laser Piezo scanning; LPF: low-pass filter; OSC: monitor oscilloscope; PI: proportional integral controller.

B. Telecom Frequency Conversion in Rubidium (Theory and Simulation)

A diamond configuration 4-level system is used for frequency conversion, see Figure 2a. The signal field (795nm) is the input which encodes the qubit information. The near resonance Pump I (780nm) and Pump II (1367nm) are

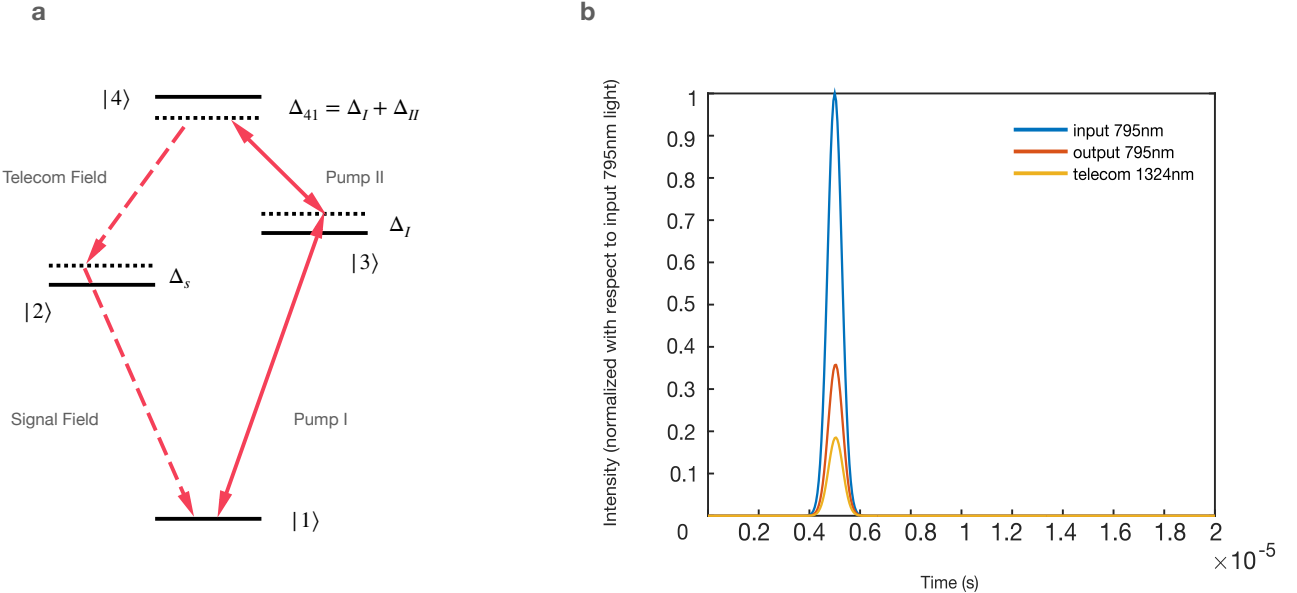


FIG. 2. a. Diamond atomic scheme use for frequency conversion and the two-photon absorption spectroscopy. In our setup $|1\rangle = ^{85}\text{Rb} : 5\text{S}_{1/2}\text{F} = 3$, $|2\rangle = ^{85}\text{Rb} : 5\text{P}_{1/2}\text{F} = 2$, $|3\rangle = ^{85}\text{Rb} : 5\text{P}_{3/2}\text{F} = 4$ and $|4\rangle = ^{85}\text{Rb} : 6\text{S}_{1/2}\text{F} = 1$. b. A simulation of the frequency conversion process using the simulation procedure described below. The two pump fields are kept at CW, the 795nm is modulated to have a Gaussian envelope using an AOM. We make an assumption that the photo detector is placed at the output port of the Rubidium cell.

strong CW pump fields. The telecom field (1324nm) is the generated field which encodes the same qubit information as that of the signal field. The Pump fields are given as

$$\vec{E}_I^{phy}(z, t) = \vec{E}_I(z) e^{-i(\omega_I t - \vec{k}_I \cdot \vec{z})} + c.c. \quad (1)$$

$$\vec{E}_{II}^{phy}(z, t) = \vec{E}_{II}(z) e^{-i(\omega_{II} t - \vec{k}_{II} \cdot \vec{z})} + c.c. \quad (2)$$

Here the $\vec{E}_I^{phy}(z, t)$ is the physical field that can be measured. The absolute value of $\vec{E}_I(z)$ is half of that of the physical field.

$$|\vec{E}_I(z)| = \frac{1}{2} |\vec{E}_I^{phy}(z, t)| \quad (3)$$

Generally $\vec{E}_I(z)$ is complex to include phase shifts. In this model we assume it to be real to simplify the modeling. Since the signal and telecom field encode qubits, they are of single photon level. They are given as

$$\hat{\vec{E}}_s^{phy}(z, t) = \vec{e}_s \left(\frac{\hbar \omega_s}{2V\epsilon_0} \right)^{\frac{1}{2}} \hat{\psi}_s(z, t) e^{-i(\omega_s t - \vec{k}_s \cdot \vec{z})} + h.c. \quad (4)$$

$$\hat{\vec{E}}_t^{phy}(z, t) = \vec{e}_t \left(\frac{\hbar \omega_t}{2V\epsilon_0} \right)^{\frac{1}{2}} \hat{\psi}_t(z, t) e^{-i(\omega_t t - \vec{k}_t \cdot \vec{z})} + h.c. \quad (5)$$

Here $\hat{\psi}(z, t)$ is the wave envelope.

This model works on a reduced 4 level Hilbert space. The Hamiltonian is

$$\hat{H} = \hat{H}_0 + \hat{V} \quad (6)$$

The \hat{H} is the free Hamiltonian of the four system without the interaction with all the fields. If we use the free Hamiltonian energy eigenstates $|n\rangle$ as our basis, the free Hamiltonian have the form

$$\hat{H}_0 = \begin{bmatrix} \hbar\omega_1 & 0 & 0 & 0 \\ 0 & \hbar\omega_2 & 0 & 0 \\ 0 & 0 & \hbar\omega_3 & 0 \\ 0 & 0 & 0 & \hbar\omega_4 \end{bmatrix} \quad (7)$$

The incident fields cause a perturbation \hat{V} of the form

$$\hat{V} = -\vec{d} \cdot \vec{E}^{phy} \quad (8)$$

where

$$\vec{E}^{phy} = \vec{E}_I^{phy} + \vec{E}_{II}^{phy} + \vec{E}_s^{phy} + \vec{E}_t^{phy} \quad (9)$$

and \vec{d} is the dipole operator. From our diamond configuration, the nonzero element of dipole operator are

$$\vec{d} = \begin{bmatrix} 0 & \vec{d}_{12} & \vec{d}_{13} & 0 \\ \vec{d}_{21} & 0 & 0 & \vec{d}_{24} \\ \vec{d}_{31} & 0 & 0 & \vec{d}_{34} \\ 0 & \vec{d}_{42} & \vec{d}_{43} & 0 \end{bmatrix} \quad (10)$$

To proceed, rotating wave approximation is used to simplify the Hamiltonian. First decompose the E field into positive and negative rotating part. Pump I physical field can be written as

$$\vec{E}_I^{phy}(z, t) = \vec{E}_I^+(z, t) + \vec{E}_I^-(z, t) \quad (11)$$

where

$$\vec{E}_I^+(z, t) \equiv \vec{E}_I(z) e^{-i(\omega_I t - \vec{k}_I \cdot \vec{z})} \quad (12)$$

and $\vec{E}_I^-(z, t)$ equal the complex conjugate part. Similar decomposition can be done with the dipole operator. We write the dipole operator from equation (10) as

$$\begin{aligned} \vec{d} = & \vec{d}_{12} |1\rangle \langle 2| + \vec{d}_{21} |2\rangle \langle 1| + \\ & \vec{d}_{13} |1\rangle \langle 3| + \vec{d}_{31} |3\rangle \langle 1| + \\ & \vec{d}_{24} |2\rangle \langle 4| + \vec{d}_{42} |4\rangle \langle 2| + \\ & \vec{d}_{34} |3\rangle \langle 4| + \vec{d}_{43} |4\rangle \langle 3| \end{aligned} \quad (13)$$

We can adjust the energy scale so that the energy of level 1 is the zero energy reference point. In interaction picture, the first operator on the right becomes

$$\vec{d}_{12} |1\rangle \langle 2| \rightarrow U^\dagger \vec{d}_{12} |1\rangle \langle 2| U = \vec{d}_{12} |1\rangle \langle 2| e^{-i\omega_{21}} \quad (14)$$

It contains a positively rotating phase factor, which means its expectation value contains the same phase factor, so we write

$$\begin{aligned} \vec{d}_{12}^+ & \equiv \vec{d}_{12} |1\rangle \langle 2| \\ \vec{d}_{12}^- & \equiv \vec{d}_{21} |2\rangle \langle 1| = \vec{d}_{12} |2\rangle \langle 1| \end{aligned} \quad (15)$$

Notice we assume that the matrix element of the dipole operator is real. We can achieve this by choosing the phase factor of the energy eigenkets. This is always possible because we have 4 unknown phase factors and 4 equations(difference of corresponding phase factor is zero), one for each dipole matrix element from the upper right triangular section of the matrix. Therefor a solution always exists. With our decomposition of the fields and the dipole operator, we rewrite perturbation given by equation (8) as

$$\begin{aligned} \hat{V} = & -(\vec{d}_{12}^+ + \vec{d}_{12}^- + \vec{d}_{13}^+ + \vec{d}_{13}^- + \vec{d}_{24}^+ + \vec{d}_{24}^- + \vec{d}_{34}^+ + \vec{d}_{34}^-) \cdot \\ & [\vec{E}_I^+(z, t) + \vec{E}_I^-(z, t) + \vec{E}_{II}^+(z, t) + \vec{E}_{II}^-(z, t) \\ & \vec{E}_s^+(z, t) + \vec{E}_s^-(z, t) + \vec{E}_t^+(z, t) + \vec{E}_t^-(z, t)] \end{aligned} \quad (16)$$

Notice that the dipole operator rotating with the frequency corresponds to the energy difference between levels while the field rotating with the frequency of the laser. We then make two approximations. First, only the laser detuning frequency is small enough to make a significant contribution in the Schrödinger equation; second, between different levels the frequency difference is large so that they contribute little in the Schrödinger equation. Hence laser Pump I only couples level 1 and 3, the same for other fields. With the above approximations, we can rewrite equation (16) as

$$\hat{V} = -[\vec{d}_{12} \cdot \vec{E}_s^+(z, t) + \vec{d}_{13} \cdot \vec{E}_I^+(z, t) + \vec{d}_{24} \cdot \vec{E}_t^+(z, t) + \vec{d}_{34} \cdot \vec{E}_{II}^+(z, t) + h.c] \quad (17)$$

For numerical simulation, we transform the system in rotating frame. In Schrödinger picture, we rewrite the perturbation from equation (17) in matrix form

$$\hat{V} = - \begin{bmatrix} 0 & \vec{d}_{12} \cdot \vec{E}_s(z) e^{i(\omega_s t - \vec{k}_s \cdot \vec{z})} & \vec{d}_{13} \cdot \vec{E}_I(z) e^{i(\omega_I t - \vec{k}_I \cdot \vec{z})} & 0 \\ \vec{d}_{12} \cdot \vec{E}_s(z) e^{-i(\omega_s t - \vec{k}_s \cdot \vec{z})} & 0 & 0 & \vec{d}_{24} \cdot \vec{E}_t(z) e^{i(\omega_t t - \vec{k}_t \cdot \vec{z})} \\ \vec{d}_{13} \cdot \vec{E}_I(z) e^{-i(\omega_I t - \vec{k}_I \cdot \vec{z})} & 0 & 0 & \vec{d}_{34} \cdot \vec{E}_{II}(z) e^{i(\omega_{II} t - \vec{k}_{II} \cdot \vec{z})} \\ 0 & \vec{d}_{24} \cdot \vec{E}_t(z) e^{-i(\omega_t t - \vec{k}_t \cdot \vec{z})} & \vec{d}_{34} \cdot \vec{E}_{II}(z) e^{-i(\omega_{II} t - \vec{k}_{II} \cdot \vec{z})} & 0 \end{bmatrix} \quad (18)$$

Notice that the matrix element is rotating at laser frequencies, which is of the order of Terahertz. If a computer is to simulate the model, the time steps should be shorter than the laser period, which would require too much resources. We need to eliminate the time dependence of the elements. This is achieved by going into the co-rotating frame of the lasers.

To understand the co-rotating frame, let's recall the interaction picture. In interaction picture, the states and operators are transformed by an unitary operator U , which gives a rotating phase factor to energy eigen state as $e^{-i(\omega_n t)} |n\rangle$, where ω_n is the transition frequency of level n relative to the reference level, which is the ground state usually.

The transformation to the rotating frame is very similar to the transition to interaction picture, except that the unitary operator brings a phase factor rotating at the corresponding laser frequency instead of the atomic transition frequency. In this 4 level system, we can choose level 4 as our reference level, so that the unitary operator is

$$U_R^\dagger = \begin{bmatrix} e^{-i[(\omega_I + \omega_{II})t - (\vec{k}_I + \vec{k}_{II}) \cdot \vec{z}]} & 0 & 0 & 0 \\ 0 & e^{-i(\omega_t t - \vec{k}_t \cdot \vec{z})} & 0 & 0 \\ 0 & 0 & e^{-i(\omega_{II} t - \vec{k}_{II} \cdot \vec{z})} & 0 \\ 0 & 0 & 0 & 1 \end{bmatrix} \quad (19)$$

Here the time related phase factor is enough to remove the time dependence. However, it is convenient to also remove the z dependence of the Hamiltonian. The trick is to ensure that the \vec{k} terms always have a opposite sign as the t terms is the phase factor.

Equation (19) is the Hermitian conjugate of the operator U_R that corresponds to the U in interaction picture transformation, since it is the Hermitian conjugate acts on the states

$$|\tilde{n}\rangle = U_R^\dagger |n\rangle \quad (20)$$

where the tilde means this is the ket in the rotating frame. The Hamiltonian transforms in such a way to preserve the Shrödinger equation of the rotating frame states.

$$\tilde{H} = U_R^\dagger H U_R + i\hbar(\partial_t U_R^\dagger) U_R \quad (21)$$

We want to preserve the Schrödinger euqation because the master equation of the density matrix is based on the Schrödinger equation.

The Hamiltonian in rotating frame is

$$\tilde{H} = \hbar \begin{bmatrix} \omega_1 + \omega_{II} + \omega_I & -e^{i\phi} \Omega_s & -\Omega_I & 0 \\ -e^{-i\phi} \Omega_s & \omega_2 + \omega_t & 0 & -\Omega_t \\ -\Omega_I & 0 & \omega_3 + \omega_{II} & -\Omega_{II} \\ 0 & -\Omega_t & -\Omega_{II} & \omega_4 \end{bmatrix} \quad (22)$$

where

$$\phi = (-\vec{k}_I + \vec{k}_{II} + \vec{k}_s - \vec{k}_t) \cdot \vec{z} + (\omega_I - \omega_{II} - \omega_s + \omega_t)t \quad (23)$$

and

$$\begin{aligned}\Omega_I(z) &\equiv \frac{\vec{E}_I(z) \cdot \vec{d}_{13}}{\hbar} \\ \Omega_{II}(z) &\equiv \frac{\vec{E}_{II}(z) \cdot \vec{d}_{34}}{\hbar}\end{aligned}\tag{24}$$

are the laser Rabi frequencies,

$$\begin{aligned}\Omega_s(z) &\equiv \frac{1}{\hbar} \left(\frac{\hbar\omega_s}{2V\epsilon_0} \right)^{\frac{1}{2}} \vec{e}_s \cdot \vec{d}_{12} \\ \Omega_t(z) &\equiv \frac{1}{\hbar} \left(\frac{\hbar\omega_t}{2V\epsilon_0} \right)^{\frac{1}{2}} \vec{e}_t \cdot \vec{d}_{24}\end{aligned}\tag{25}$$

are the single photon Rabi frequencies.

We can further simplify the Hamiltonian. First the generated telecom photon must satisfy the energy conservation and momentum conservation

$$\omega_s + \omega_{II} = \omega_t + \omega_I\tag{26}$$

$$\vec{k}_s + \vec{k}_{II} = \vec{k}_t + \vec{k}_I\tag{27}$$

use these relation we find the phase factor in equation (23) is $\phi = 0$. Second, the calculation is not changed if we change the reference energy level. This is achieved by adding multiples of identity operator to \tilde{H} . Notice we can do this even if we are in rotating frame but not in Schrödinger picture. This is because the transformation given by equation (21) does not change the diagonal elements of the original H , up to some constants introduced by the second term on the right of equation (21). If we add αI to \tilde{H} , it is the same if we add αI to H first, then perform the transformation given by equation (21). Here, we want to use the laser detunings to express frequencies on the diagonal elements, so we add $-(\omega_1 + \omega_{II} + \omega_s)\hat{I}$ to \tilde{H}

$$\tilde{H} = \hbar \begin{bmatrix} 0 & -\Omega_s & -\Omega_I & 0 \\ -\Omega_s & -\Delta_s & 0 & -\Omega_t \\ -\Omega_I & 0 & -\Delta_I & -\Omega_{II} \\ 0 & -\Omega_t & -\Omega_{II} & -\Delta_{41} \end{bmatrix}\tag{28}$$

where $\Delta_s = \omega_s - (\omega_2 - \omega_1)$, $\Delta_I = \omega_I - (\omega_3 - \omega_1)$, $\Delta_{II} = \omega_{II} - (\omega_4 - \omega_3)$ are the one-photon detunings and $\Delta_{41} = \Delta_I + \Delta_{II}$ is the two-photon detuning.

From equation (20) the density matrix in the rotating frame is

$$\tilde{\rho} = U_R^\dagger \rho U_R\tag{29}$$

or express ρ in terms of $\tilde{\rho}$,

$$\rho = U_R \tilde{\rho} U_R^\dagger\tag{30}$$

where ρ is the original density matrix in Schrödinger Picture. The evolution of the rotating frame density matrix is governed by the master equation

$$\dot{\tilde{\rho}} = -i[\tilde{H}, \tilde{\rho}] + \sum_{a>0} (L_a \tilde{\rho} L_a^\dagger - \frac{1}{2} L_a^\dagger L_a \tilde{\rho} - \frac{1}{2} \tilde{\rho} L_a^\dagger L_a)\tag{31}$$

The polarization of the medium is

$$\vec{P} = n \text{Tr}(\rho \vec{d})\tag{32}$$

and the light propagation is governed by

$$(\nabla^2 - \frac{1}{c^2} \frac{\partial^2}{\partial t^2}) \vec{E} = \mu_0 \frac{\partial^2 \vec{P}}{\partial t^2}\tag{33}$$

substitute Eq(4),(5) and (32) into Eq(33), matching the terms with the same rotating frequency

$$\left(\frac{\partial}{\partial t} + c \frac{\partial}{\partial z}\right) \vec{\psi}_s(z, t) = i \frac{\omega_s n V}{\epsilon_0} \tilde{\rho}_{21} \vec{d}_{12} \quad (34)$$

$$\left(\frac{\partial}{\partial t} + c \frac{\partial}{\partial z}\right) \vec{\psi}_t(z, t) = i \frac{\omega_t n V}{\epsilon_0} \tilde{\rho}_{42} \vec{d}_{24} \quad (35)$$

These are the equations couple the atomic states to the field envelopes. Together with Eq (31), the three equations fully describe the conversion process. We conduct a numerical simulation to investigate the frequency response of the conversion process. In the simulation we apply several simplifications. We only consider an effective four-level system and ignore the effects from all hyperfine structures. We also completely ignore the Doppler effect from the motion of the atoms. We simulate a 7cm long cell, the beam diameter is 0.29mm and the atomic density is $4 \times 10^{17}/m^3$. We set the 780nm and 1367nm pump to be CW light and the signal 795nm to be a Gaussian pulse. We found that the conversion efficiency, which is defined as the ratio of the converted 1324nm intensity to the incident 795nm light intensity, is very sensitive to the choice of the dipole moments. Since we ignore all the hyperfine levels, we do not expect an accurate conversion efficiency from the numerical simulation. Figure 2b shows a typical conversion process from the numerical simulation. We calculate the conversion efficiency as a function of the detunings of the two pump fields, the results is show in Fig. 3.

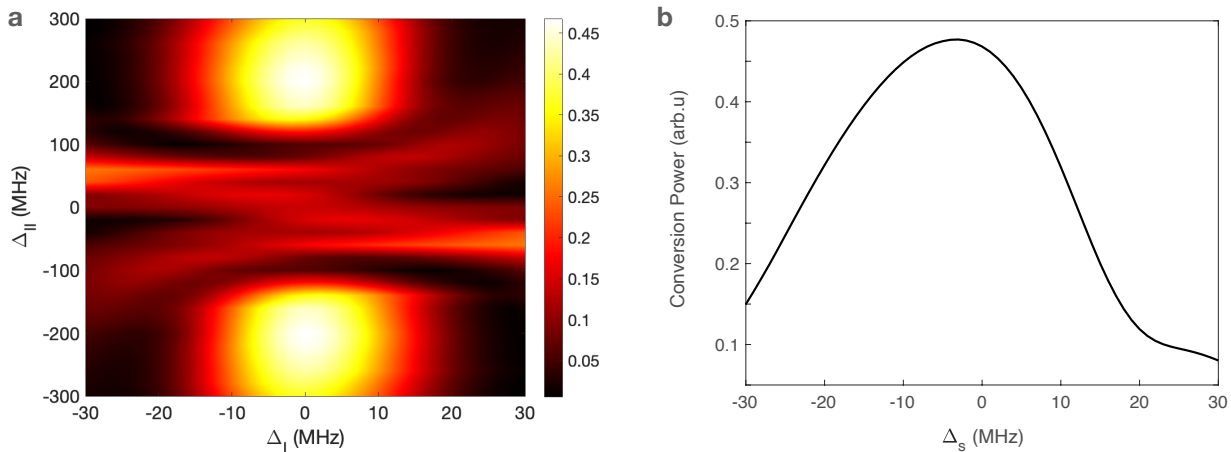


FIG. 3. Simulation results. a. Conversion output power as a function of the two pump field detunings. Here Δ_I is the 780nm pump and the Δ_{II} is the 1367nm pump. The colorbar is in arbitrary unit. In this plot $\Delta_s = 0$ MHz b. Conversion output power as a function of the signal detuning. In this plot $\Delta_I = 0$ MHz and $\Delta_{II} = 200$ MHz. The conversion power in both figure is in arb.u because they are highly dependent on the dipole moment value.

C. Telecom Frequency Conversion in Rubidium (Experiments and Charaterization)

The frequency conversion setup is shown in Fig. 4. The two pump fields and the signal 795nm beam propagate collinearly. The 795nm and the 1367nm fields are H polarized and the 780nm light is V polarized. We use a 71.8mm long Thorlabs Rubidium reference cell(GC25075-RB) maintained at a temperature of 100°C. The cell contains 5 – 10mg nature composed vapor of ^{85}Rb and ^{87}Rb . The attenuation of the 1367nm pump field is achieved by three processes. The generated 1324nm is orthogonal to the 1367nm pump field. A pair of Glan Laser Polarizer is used to filter out H polarized 1367nm field. A band-pass filter(1320nm center wavelength, FWHM 12nm) is then used. Finally, the pumps are slightly misaligned from the signal to provide a small spatial separation between the 1367nm pump and the generated 1324nm beam.

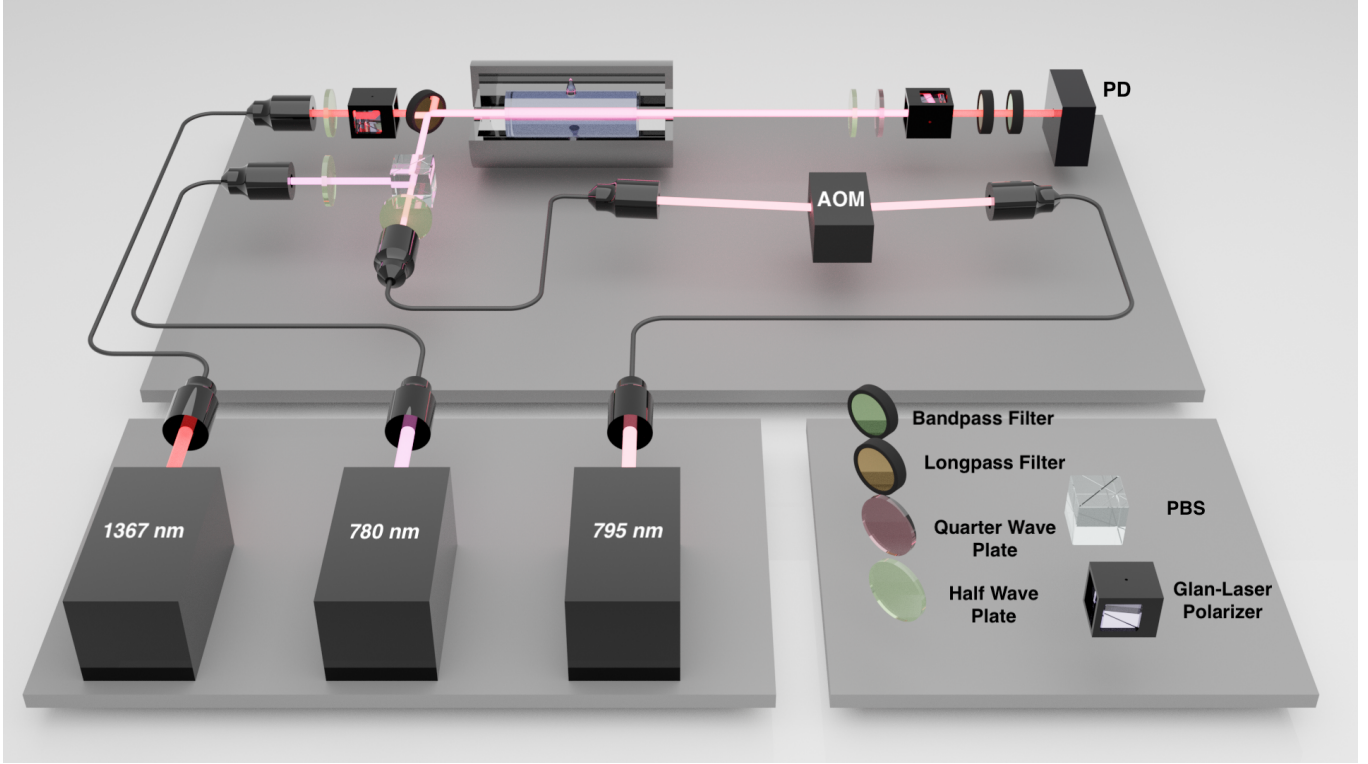


FIG. 4. The frequency conversion setup. An AOM is used to modulate the field envelope of 795nm signal. The 795nm signal is combined with 780nm pump, and is combined with the 1367nm pump by a long pass filter. We use a half-wave plate and a quarter-wave plate before the second Glan Laser Polarizer to compensate the birefringence introduced by the Rubidium cell. An InGaAs avalanche photodetector is used to detect the generated 1324nm field.

We first measure the frequency conversion efficiency by locking the 795nm laser to Rubidium Saturated Absorption Spectrum at transitions $^{85}\text{Rb} : 5\text{S}_{1/2}\text{F} = 3 \rightarrow 5\text{P}_{1/2}\text{F}' = 2$ and the 780nm laser at $^{85}\text{Rb} : 5\text{S}_{1/2}\text{F} = 3 \rightarrow 5\text{P}_{3/2}\text{F}' = 4$. We then lock the 1367nm laser to the $5\text{P}_{3/2}\text{F}' = 4 - 6\text{S}_{1/2}\text{F}' = 3$ transition using the two-photon absorption spectrum. We can also modulate the 795nm into pulse envelopes using the AOM. The conversion efficiency is measured to be around 0.1%. We then lock the 795nm to $^{85}\text{Rb} : 5\text{S}_{1/2}\text{F} = 3 \rightarrow 5\text{P}_{3/2}\text{F}' = 4$ transition and scan the 780nm pump across transition $^{85}\text{Rb} : 5\text{S}_{1/2}\text{F} = 3 \rightarrow 5\text{P}_{1/2}\text{F}' = 2$ at 10.1 Hz and scan the 1367nm pump across transition $5\text{P}_{3/2}\text{F}' = 4 - 6\text{S}_{1/2}\text{F}' = 3$ at 10 Hz. We record the reading of the photodetector in an oscilloscope and obtain the conversion intensity as a function of the pump fields detunings, as shown in Figure 5.

III. LONG DISTANCE QUANTUM NETWORK INFRASTRUCTURE

A. Long Distance Fiber Infrastructure

A practical quantum network, used to interconnect quantum systems over large distances in real-world configurations, needs to co-exist and be compatible to the largest degree possible with existing classical telecommunication network infrastructure. This is the litmus test for bringing quantum networking technology out of the confines of a laboratory without the requirement of a new infrastructure that can be prohibitively costly. Furthermore, the co-existence of quantum and classical signals is an open research topic. While it is feasible to create fully transparent, all-optical, quantum networks utilizing the available dark fiber infrastructure and use separate channels for quantum and classical traffic, extensive research is required to determine if and how it would be possible to have quantum and classical signals share the same optical fibers while avoiding significant cross-talk and reliably maintaining the quantum information over long distances.

The SBU/BNL quantum network prototype interconnects quantum laboratories at SBU and BNL, taking advantage of the existing optical fiber infrastructure within the campuses and a commercially available long-distance optical fiber links. There are four single-mode fiber strands available that are used for quantum and classical signals, enabling

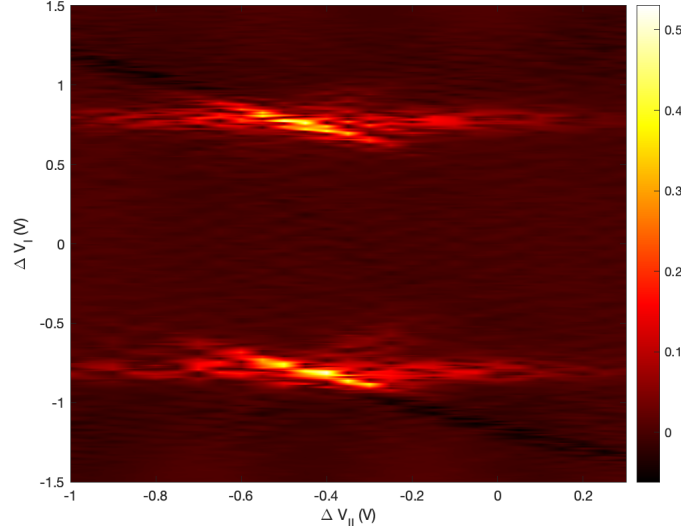


FIG. 5. The measured conversion intensity as a function of the pump fields laser Pizeo voltage offset. The colorbar is in arbitrary unit. In a coarse approximation, the Pizeo voltage offset can be regarded as linear to the frequency detuning. However, more in depth calibration should be done to translate the voltage offset to frequency detunings. The zero point of the voltage offset does not necessary corresponds to the zero detuning position. The graininess is due to the limited data points density.

a wide range of experiments. We utilize dedicated dark fibers for the quantum signals while all classical signals are carried in separate classical-signal-only fibers, except for the polarization reference frames, which co-propagate with the qubits. The long-distance fiber link provides connectivity between the main networking hub at each campus with an average attenuation of approx. 22.7dB at 1310nm. It consists of a long segment and a shorter one, comprising multiple fusion-spliced shorter segments, patched together in a co-location room near the SBU campus. At SBU and BNL, the long-distance fibers are patched to the local infrastructure fibers that interconnect the various campus buildings. At both SBU and BNL, these fibers comprise multiple segments, fusion and/or mechanically spliced, as well as fiber patches between distribution frames. At SBU, the fiber path runs from the university's main networking hub (ECC building) to the Physics building's QIT lab. At BNL, the fiber path also runs from the main networking hub (ITD building) to the QIST lab in the Instrumentation Division building. In addition to the overall physical length one must also account for the patch fibers within the networking hubs and the patch fibers from the fiber panels within each quantum lab to the quantum memories and detectors. Overall, the physical fiber length from Alice to Bob through Charlie is estimated at approximately 140km; however, the total measured loss is 23dB, corresponding to a perfect fiber length (with a typical loss of 0.35dB/km at 1310nm) to over 160km.

B. Polarization Compensation

Since in quantum networking applications, the quantum information is often encoded in the polarization state (SOP) of photons, a particular bottleneck in these long-distance applications is that of polarization fluctuations, which is rarely of concern in classical telecommunication networks. If fibers were perfect (e.g. polarization-maintaining), the signal SOP would remain mostly constant, eliminating the need for compensation. However, millions of miles of deployed non-polarization maintaining fiber infrastructure already exist and should be utilized given the requirements needed for entanglement communication. In these optical fibers the SOP of the light propagating varies along its length due to random birefringence induced by thermal changes, mechanical stress, or fiber core irregularities and other changing environmental and material inhomogeneities - influencing both polarization axes simultaneously. These fluctuations can also lead to variations in the optical path length, resulting in fluctuations/drift of power. We have established the dynamic compensation of polarization drift to maintain quantum information integrity. Here we use a quantum-state compensator for flying photons to maintain their polarization, ensuring that transmitted qubits' purity is optimal at their destination/measurement station. The SOP can be changed using compensation retardation plates or by actively modifying the birefringence in the optical fiber, as was performed here. Our experiment uses a prototype of a machine learning enhanced polarization compensating device built by Qunnect Inc (Qu-APC module). The module requires a triggered string of reference photons interspersed between the qubit carrying photons. The method has the advantage of measuring the polarization of photons at the same transmission wavelength as the qubits.

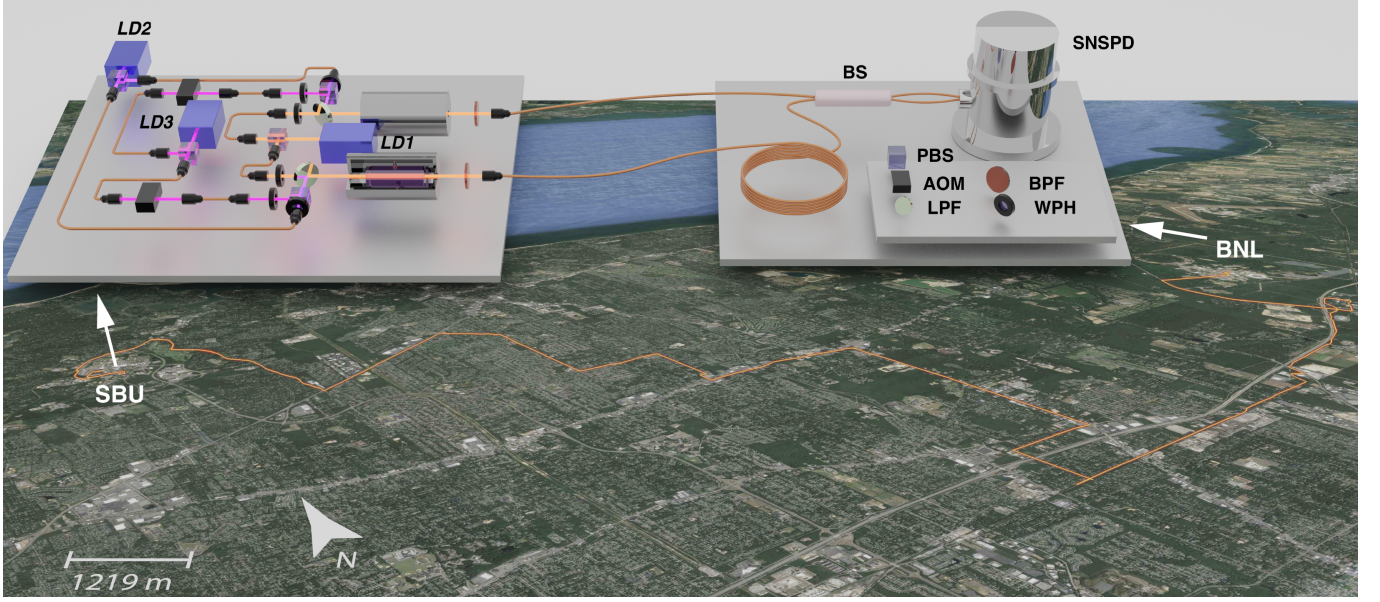


FIG. 6. Overview of the testbed on Long Island, New York. It consists of 4 commercially available fibers (rented from Crown Castle) connecting the main fiber exchange points in Stony Brook University (ECC Engineering Building) and Brookhaven National Laboratory (SDCC Building). From ECC, several fiber strands connect to the Quantum Internet Laboratory (QIT) in the Physics and Astronomy Building. From SDCC, several strands connect to the Quantum Information Science and Technology Laboratory (QIST) in the Instrumentation Building. Two quantum memories and frequency conversion setups (Alice and Bob) are located on the SBU QIT laboratory and are connected independently to the network. The interference setup and telecom compatible single photon nano-wire detectors (Charlie station) are located in the QIST laboratory in BNL. The other two fibers are used to transport classical timing triggers, network status, and sequencing information.

The polarization controller itself consists of three motorized rotating paddles with fiber loops acting as wave-plates on each of the Alice and Bob branches to rotate the light's polarization-state with feedback from a polarimeter capable of remapping the light's SOP down to -70dB. The retardation plates effectively rotate around the optical beam (fiber) with respect to each other, inducing strain on the fiber, and changing the polarization of the photons travelling through.

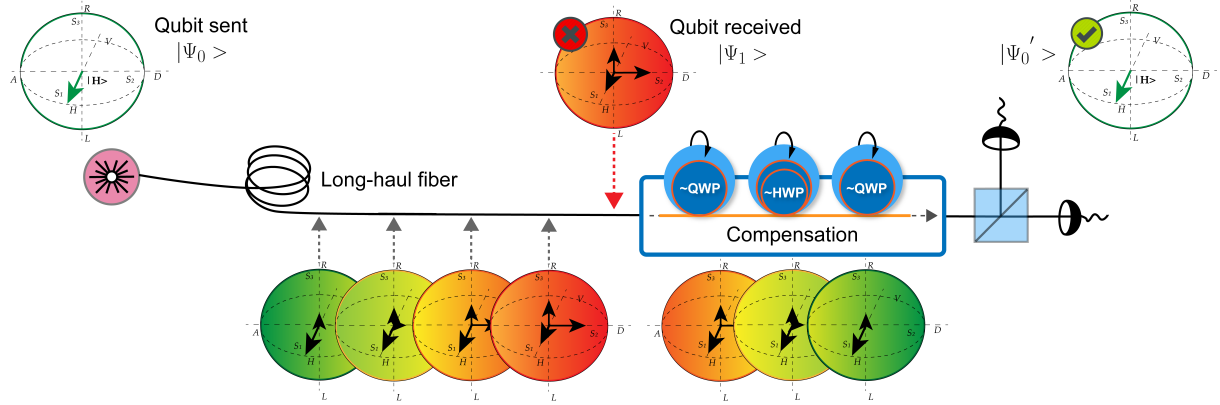


FIG. 7. Principle of operation for polarization compensation. The initial qubit polarization is represented by the green vector mapped onto a sphere. As the H qubit (left) transmits through the fiber, fluctuations in the birefringence cause the polarization to drift (defined as the product of the 3 Stokes vectors shown in black) from its initial state (trending towards red). The compensation device modulates the fiber stress to compensate for this drift and restore the initial state (right).

Using rotating wave-plates allows to easily correct for the random polarization drifts by letting the state randomly “walk-off” within a specific interval before correcting for it. Therefore, at every acquisition cycle, Alice sends a “calibration start” trigger along with CW polarized light at -65bB (receiving end). Polarization compensation setup

then adjusts both branches to the same chosen polarization at the measurement station. Once the two have converged within an acceptable margin of the desired state, it sends back to Alice a “calibration termination”. Then Alice confirms as she sends qubits back instead of CW light (corresponding to the “calibration stop”). The more frequent the calibration is applied, the less time it takes to converge, but the less network uptime is available. For optimal results and maximal network uptime, the re-calibration was re-applied every 5 minutes by which time the drift was too large to continue the interference with sufficient visibility. Figure 7 shows the effect of the polarization compensation on an interference observed after the 68km propagation in both branches.

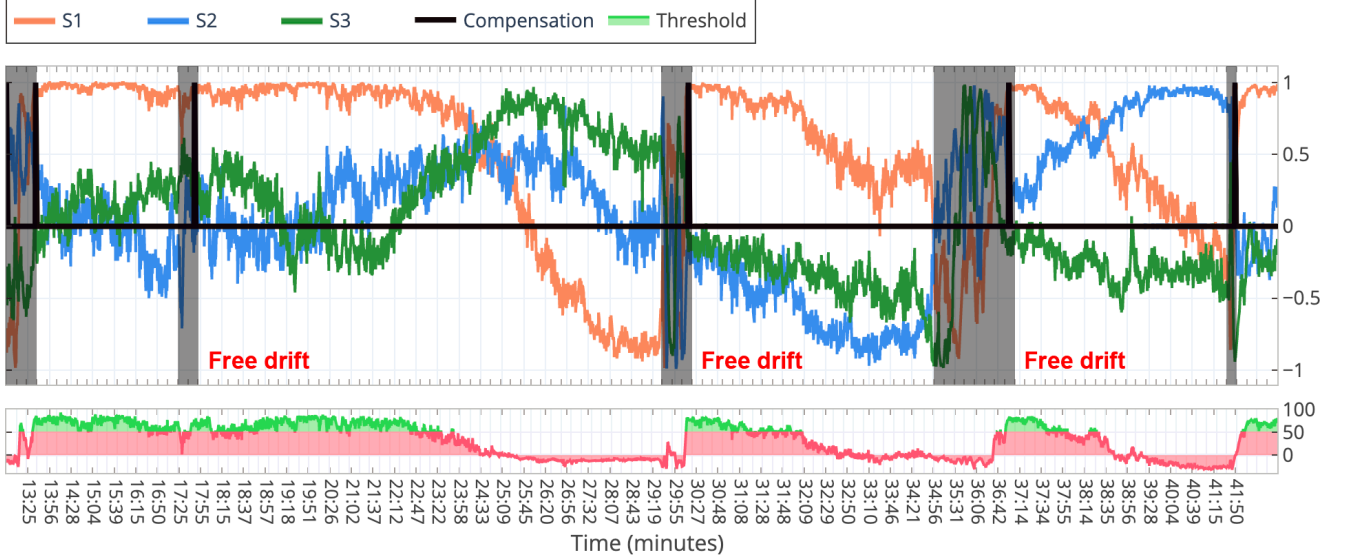


FIG. 8. Top: State compensation for out-of-cycle polarization basis realignment showing the three normalized Stokes vectors S1, S2, and S3 as a function of time. Here the Qu-APC device is active and cycling its compensation routine. Grey periods correspond to when the compensation system is active (network down-time), whereas periods in between correspond to free drift. Bottom: Compensation score indicating the state of the drift and the expected need for recalibration. We observe that without compensation, on average, the available window for experiments is on the order of 2-5-minutes before the drift impends the results (red). With the calibration above threshold (green), the post-stabilized visibility at the interferometer was roughly constant at 88%.

C. Charlie station at Brookhaven

At the Charlie station in BNL, a series of additional wave-plates are used to compensate for polarization rotation caused by propagation in the lab optical fibers after the compensation apparatus. Then the pulses retrieved from the two paths interfere at a 50 : 50 NPBS beamsplitter, and then go to two single-photon detectors placed in another adjacent laboratory through 10m light-shielded fibers. These detectors generate a signal every time they record a hit. Data is then analyzed to calculate the coincidence rate between the two output arms of the interferometer.

IV. LONG DISTANCE QUANTUM INTERFERENCE EXPERIMENTS

Having quantum memories operating at telecom wavelengths and a long-distance fiber infrastructure that does not degrade the initial quantum states, allow us to connect the two quantum light matter interfaces. We now show quantum interference experiments using the large interferometer connecting SBU and BNL. Firstly, we present a single photon (SP) Mach-Zehnder interferometer demonstrating the preservation of quantum state transmitted over a 140 km network. Secondly, we present a two-photon (TP) Hong-Ou-Mandel interference experiment, showing the indistinguishability of the telecom photons produced in the quantum memories and the possibility to create entanglement between them. We mention that first experiments connecting telecom operational light-matter interfaces and telecom optical links have been shown recently [34–36]. However, the experiments presented here are covering an unprecedented distance, one order of magnitude larger than anything attempted before.

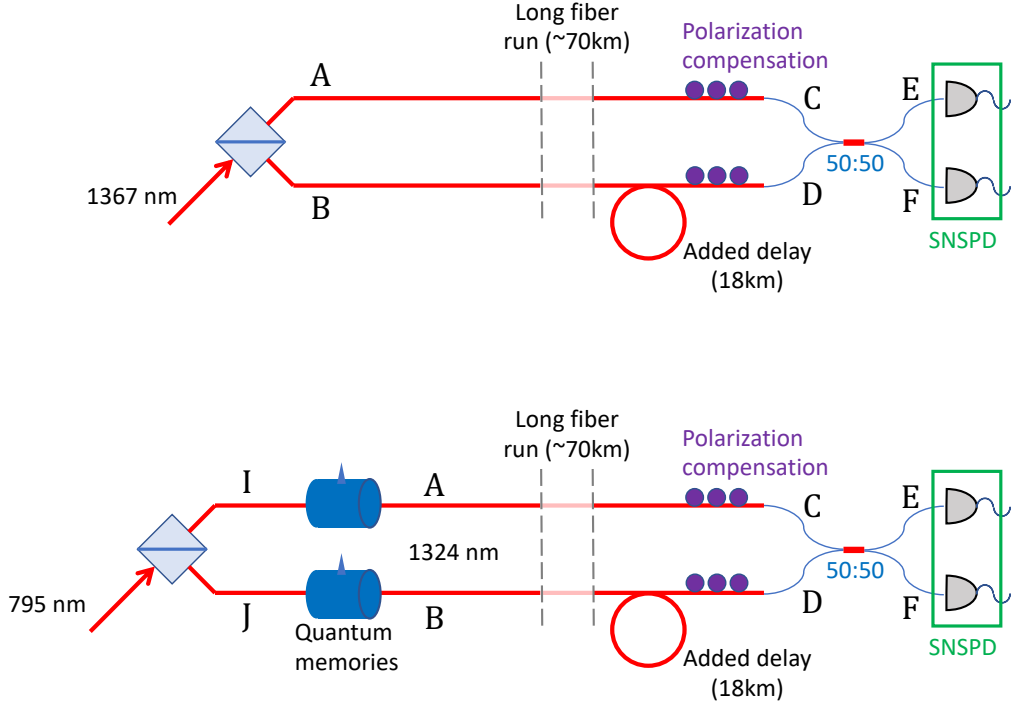


FIG. 9. Basic schematic diagrams of the long-distance interference experiments. *Top*: The 1367 nm coherent beam at SBU is split and sent down the two long fiber runs; for single-photon running the initial beam is heavily attenuated. At the receiving end at BNL the two lines are combined through a beam splitter whose outputs go to two detectors. The paths are equal length for the MZ configuration, and an extra 18 km loop is added to one path for the HOM configuration. *Bottom*: The input 795 nm beam is split and then sent to two quantum memories, where it is combined with 1367 nm and 780 nm beams (not shown) and converted to 1324 nm light, which is then sent on to the two long fiber runs.

V. SINGLE PHOTON (SP) MACH-ZEHNDER INTERFEROMETRY

The simplest experiment to demonstrate interference after transmission on two long-distance links is to split a low-intensity beam at the transmitting station, and then re-combine them through a splitter at the receiving station. The basic arrangement is shown in Figure 9 and corresponds to a Mach-Zehnder interferometer with one spatial mode in the fibers.

With a narrow-band laser source we can write the initial state I of the field before the initial symmetric beamsplitter as a coherent, polarized, quasi-monochromatic state $|\alpha\rangle_{I,s}$ where s labels the polarization of the occupied mode. We can then write the state of the two modes A and B after the splitter as

$$\Psi_{AB} = \frac{1}{\sqrt{2}} |\alpha\rangle_{A,s} \otimes \frac{1}{\sqrt{2}} |\alpha\rangle_{B,s} \quad (36)$$

After transmission the state of the modes at points C and D are still coherent but attenuated

$$\Psi_{CD} = \frac{t_{AC}}{\sqrt{2}} |\alpha\rangle_{C,p} \otimes \frac{e^{i\phi} t_{BD}}{\sqrt{2}} |\alpha\rangle_{D,q} \quad (37)$$

where (i) the intensities along the $A \rightarrow C$ and $B \rightarrow D$ are reduced by (real) transmission coefficients $T_{AC} = t_{AC}^2$ and $T_{BD} = t_{BD}^2$, respectively; (ii) the factor $e^{i\phi}$ encodes any phase difference resulting from any length differences between the two long fibers; and (iii) the polarizations of the modes occupied after transmission are denoted p and q ; in the absence of polarization compensation the transforms $s \rightarrow p$ and $s \rightarrow q$ will generally be random.

The state in the modes E and F after the final beamsplitter then becomes

$$\Psi_{EF} = \left(\frac{t_{AC}}{2} |\alpha\rangle_{E,p} + \frac{e^{i\phi} t_{BD}}{2} |\alpha\rangle_{E,q} \right) \otimes \left(\frac{t_{AC}}{2} |\alpha\rangle_{F,p} - \frac{e^{i\phi} t_{BD}}{2} |\alpha\rangle_{F,q} \right) \quad (38)$$

From standard photo-detection theory we can now calculate the rates of detectable photons in E and F at any specific time as

$$R_E(t) = \frac{|\alpha|^2}{2} \frac{T_{AC} + T_{BD}}{2} (1 + \mathcal{V} \cos \phi(t)) \quad R_F(t) = \frac{|\alpha|^2}{2} \frac{T_{AC} + T_{BD}}{2} (1 - \mathcal{V} \cos \phi(t)) \quad (39)$$

where $|\alpha|^2$ is the original beam intensity in photons per coherence time, $(T_{AC} + T_{BD})/2$ is the average transmission through the two fiber runs. This is the standard Mach-Zehnder interference for a macroscopic beam in a single spatial mode, where the intensities at the two outputs are directly anti-correlated. It is interesting to note, that even though the entangled state is travelling through both fibers, the loss in photon intensity corresponds to only the average loss in a single fiber and not the product of two losses.

Here \mathcal{V} is the *visibility* of the M-Z interference pattern

$$\mathcal{V} \equiv \frac{2}{t_{AC}/t_{BD} + t_{BD}/t_{AC}} |\langle p|q \rangle| = \frac{1}{\cosh(\log(t_{AC}/t_{BD}))} |\langle p|q \rangle| \quad (40)$$

The first factor relates to the balance between the transmission losses along the two fiber runs, and the second factor is the magnitude of the overlap between the two final polarization states p and q . If the beams are balanced on arrival and the polarization states are the same then the visibility will be unity; as either of these is not satisfied then the visibility will decrease.

A. Single-photon interference

The anti-correlated intensities described in Equation 39 are true for any coherent state, with any intensity $|\alpha|^2$. However, for beams at the single-photon level the M-Z interferometer can be seen as transporting an entangled state along macroscopic distances.

The coherent beam state as defined by Glauber can be expanded in a Fock basis as

$$|\alpha\rangle = e^{-|\alpha|^2} \sum_n \frac{\alpha^n}{\sqrt{n!}} |n\rangle \quad (41)$$

with the average occupation number of state $|\alpha\rangle$ being $\langle n \rangle = |\alpha|^2$. For a purely monochromatic beam this would be the number of photons in the mode over infinite time; for a quasi-monochromatic beam it can be taken to represent the number of photons in the beam per interval of the coherence time, as above.

For a weak, highly attenuated initial beam $|\alpha|^2 \ll 1$ and so we can expand Equation 36 as

$$\Psi_{AB} = \frac{e^{-|\alpha|^2}}{\sqrt{2}} \left(|0\rangle_{A,s} + \alpha |1\rangle_{A,s} + \mathcal{O}(\alpha^2) \right) \otimes \frac{e^{-|\alpha|^2}}{\sqrt{2}} \left(|0\rangle_{B,s} + \alpha |1\rangle_{B,s} + \mathcal{O}(\alpha^2) \right) \quad (42)$$

Limiting our observations to the cases where at least one photon is detected effectively post-selects against the $|0\rangle_{A,s} \otimes |0\rangle_{B,s}$ branch of the wavefunction. Expanding the reduced wavefunction to leading order in α we have

$$\Psi_{AB} = \frac{\alpha}{\sqrt{2}} \left(|1\rangle_{A,s} \otimes |0\rangle_{B,s} + |0\rangle_{A,s} \otimes |1\rangle_{B,s} \right) \quad (43)$$

Equation 43 is then an entangled state, a superposition between a single photon having gone down the A channel and the B channel. If we can observe an interference between the two terms at the receiving end then we confirm that the entangled superposition is preserved in transit, i.e. no “which-way” information was available to the outside world.

If the state we Ψ_{AB} in Eq. 43 propagated through the fiber transmission and the beamsplitter without decoherence or interaction with the outside world, then as in Sec. V we can derive the (complementary) probabilities of seeing a photon at E versus F , conditioned on a photon having been observed at one or the other:

$$P_E(t) = \frac{1}{2} (1 + \mathcal{V} \cos \phi(t)) \quad P_F(t) = \frac{1}{2} (1 - \mathcal{V} \cos \phi(t)) \quad (44)$$

Here the visibility \mathcal{V} is the same as shown in Eq. 38. If we can show that these probabilities are observed in the single-photon limit then it will confirm that transmission over the long fibers preserves the entangled state in Equation 43. By contrast, if the state were to de-cohere, de-polarize or otherwise interact non-reversibly with the environment then the interference would not manifest and the observation probabilities would reduce to $P_E = P_F = 1/2$.

It may not be straightforward to measure the probabilities of Eq. 44 directly if the photon rates are low and the phase difference $\phi(t)$ is changing quickly. We can instead create a correlation observable, following the simple idea that if photons are, say, generally being steered toward output E then to photons observed close together in time will both tend to register at E ; and this will generate a net suppression in observing E - F pairs which are close together in time.

With individual photon detection we measure the standard normalized correlation function

$$G^{(2)}(\Delta t) \equiv \frac{\langle P_E(t)P_F(t + \Delta t) \rangle_t}{\langle P_E(t) \rangle_t \langle P_F(t + \Delta t) \rangle_t} \quad (45)$$

With Equation 44 this becomes for the Mach-Zehnder configuration

$$G^{(2)}(\Delta t) = 1 - \mathcal{V}^2 \langle \cos(\phi(t)) \cdot \cos(\phi(t + \Delta t)) \rangle_t = 1 - \mathcal{V}^2/2 \text{ for } \Delta t \rightarrow 0 \text{ or } 1, \text{ for large } \Delta t \quad (46)$$

and so if the coherence between the two branches of the superposition is preserved then we would expect to observe a dip feature in the $G^{(2)}(\Delta t)$, with a maximum depth of 1/2 for unit visibility; and then a return to $G^{(2)} = 1$ when Δt is much larger than the time scale on which $\phi(t)$ is fluctuating. It should be noted that this anti-correlation between two photon detections is *not* a two-photon interference effect; it is rather the correlation in time between two single-photon interference effects. We will examine true two-photon interference in Section VI below.

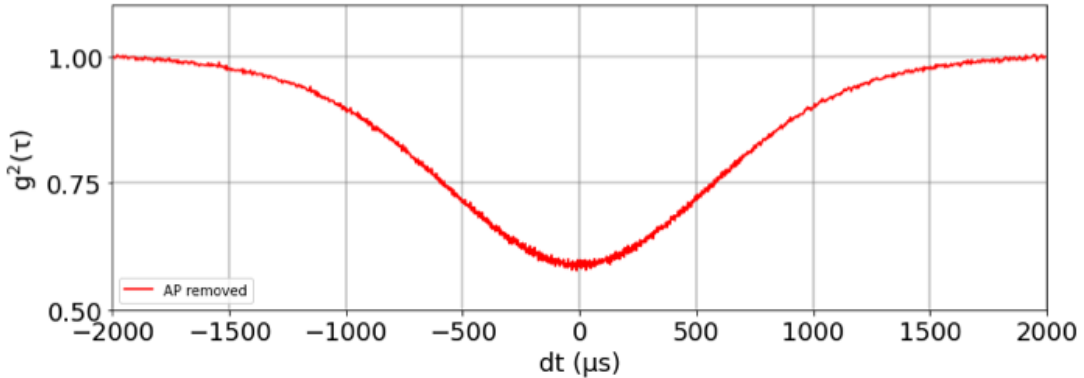


FIG. 10. Measured $G^{(2)}$ correlation function between single-photon detections at the two outputs of the final beamsplitter in the Mach-Zehnder configuration. Here we are observing 1324 nm photons which have been produced by a 795 nm photon being split and then converted in two quantum memories, as in Figure 9. The dip follows the expectation from Equation 46, with a visibility of about $\mathcal{V} = 0.9$ and a feature width of about a millisecond.

Figure 10 shows the $G^{(2)}(\Delta t)$ correlation function between single-photon hits detected at the two output channels of the final beamsplitter, in the M-Z configuration, as a function of the time separation between the detected hits. A clear anti-correlation is seen for small Δt , and a return to $G^{(2)} = 1$ at large Δt , exactly as expected from Equation 46. The feature's width measures the timescale on which the induced phase difference $\phi(t)$ is varying, here on the order of a milliseconds. These data were taken with polarization optimization at the receiving end. The dip has a minimum value of about $G^{(2)} = 0.6$, indicating to a very high visibility of $\mathcal{V} \sim 0.9$ and so a correspondingly good match between the final polarizations.

The interference results in Figure 10 were measured with 1324 nm light, as shown in the lower panel of Figure 9. Thus, in this experiment the first entangled state of the type shown in Equation 43 is present with the 795 nm photons at the initial mode points I and J . That superposition state is then put through frequency conversion to 1324 nm light in the two quantum memory vapor cells, to emerge at mode points A and B before being sent onto the long fiber runs. The fact that the Mach-Zehnder interference is observed with high visibility at the receiving end indicates that the entangled superposition is well preserved through *both* the conversion process and the long-distance transmission stage.

VI. TWO-PHOTON (TP) HONG-OU-MANDEL INTERFEROMETRY

To demonstrate that our memories are capable of being entangled by measurement, we must demonstrate that the quantum information is preserved after frequency conversion, retrieval and long distance transmission. The application

of the Cabrillo entanglement scheme requires that the temporal envelope, optical frequency, and polarization of both photon streams produced in the Alice and Bob stations remain indistinguishable at the input of the interference experiment. Therefore, we calibrate the relevant parameters of the quantum memories to ensure that Alice and Bob have identical FWM bandwidths and conversion efficiencies. Two independent filtering systems (to filter out the auxiliary frequency conversion fields) located after the atomic interfaces, each consisting of several consecutive wavelength filters, are calibrated to have identical transmissions for Alice and Bob. After carefully matching all the auxiliary fields parameters, we proceed to frequency convert qubits at the few-photon level in the two memories and couple their output into the long distance fibers.

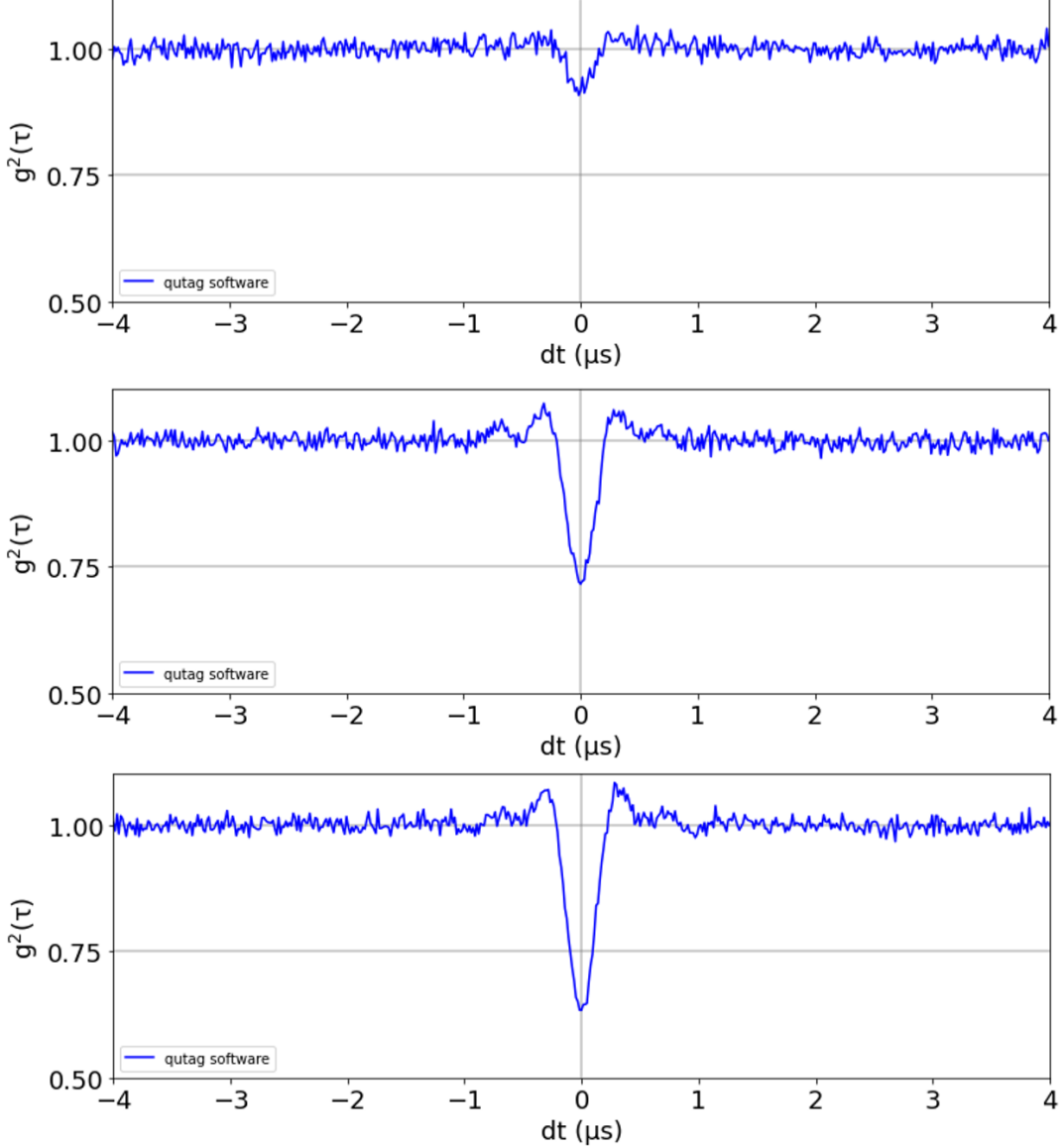


FIG. 11. Correlation $G^{(2)}(\Delta t)$ measurements between single-photon detections of 1324 nm light produced through frequency conversion, as per the lower panel of Figure 9. These were taken in the HOM configuration with the extra delay loop on one path; this delay is much longer than the coherence time of the 1324 nm beam and so ensures that the photons arriving at the receiver are mutually incoherent. We observe the Hong-Ou-Mandel (HOM) interference, manifested as a depletion of observed pairs at the beamsplitter output ports, when the detection time difference is on the order of the beam coherence time. *Upper:* The magnitude of the HOM dip is small when the polarization compensation is deliberately set badly. *Middle:* Without any polarization adjustment the HOM dip reaches a minimum of $G^{(2)} = 0.75$, which is typical for a random alignment. *Lower:* With optimization in polarization compensation the HOM minimum is as low as $G^{(2)} = 0.65$ indicating a high degree of indistinguishability between the arriving photons.

The mean number of photons per pulse at the output of each memory is measured to be $\langle n \rangle_{\text{Alice}} = 20$ and $\langle n \rangle_{\text{Bob}} = 20$. As indicated in Fig. 9, in this experiment we add a 18km long delay on the BNL side in order to scramble the phase coherence and measure the second order correlation. The losses through both the long distance setups is measured to be $\approx 23\text{dB}$ for one link and $\approx 26\text{dB}$ for the longer arm. We obtain average photon numbers after long distance propagation of $\langle n \rangle_{\text{Alice}} \approx 0.1$ and $\langle n \rangle_{\text{Bob}} \approx 0.06$ at the nanowire detectors in BNL. The HOM coincidence rate is measured versus the arrival time of the photons in the two detectors. The coincidences within a temporal region of interest (ROI) are post-selected with a width of $0.1\mu\text{s}$. We observe the desired modulation in the coincidence rate, exhibiting a minimum for the initial identical polarization and reaching a maximum corresponding to uncorrelated photons beyond the coherence time of the FWM process. The interference visibility is measured to be $V = (38 \pm 2.0)\%$. We conclude that our memories do not significantly affect the indistinguishability of the photons.

VII. DISCUSSION AND OUTLOOK

Our experimental scheme reflects the original idea of the Cabrillo scheme [21], where entanglement is produced based on a measurement projection, applied in a long distance 158 km network. In our case, the two atomic quantum memories are initially prepared in the in $|1\rangle$ states (ground state in Fig. 2). The 795 nm weak excitation pulse, together with the FWM pump beams excites the atoms to state $|4\rangle$ (excited state in Fig. 2). The atoms can then decay to the intermediate state $|2\rangle$ by spontaneous emission (creating the 1324 nm photons), with a small probability given by the efficiency of the FWM process. After the photons propagation in the long distance links, the detection of one photon in either detector after the HOM interference projects the state of the two memories to $|\phi\rangle = \frac{1}{\sqrt{2}}(|12\rangle + e^{i\theta}|21\rangle)$. The phase θ is due to the phase difference of the weak excitation pulses applied to the two memories and the memory-detector path difference. Future experiments will aim to store these entangled state of the memories. An important constrain will be to have long coherence times on the order of hundreds of microseconds, allowing for the long-distance transmission of the telecom photons and the heralding information transmission. With these conditions it will be possible to verify the entanglement created between the memories by retrieving their state into an entangled photonic state and reconstructing its density matrix.

VIII. ACKNOWLEDGEMENTS

This work is supported by the Department Of Energy ASCR grant: “Inter-campus network enabled by atomic quantum repeater nodes”, the Department Of Energy CESER grant: “A Prototype for Ultimate Secure Transmission” and the Brookhaven National Laboratory LDRD grant, “Building a quantum repeater prototype connecting BNL to NYC”.

IX. REFERENCES

- [1] A. Acin, et al., The quantum technologies roadmap: a European community view, *New J. Phys.* 20 080201 (2018).
- [2] C. Simon. Towards a global quantum network, *Nat. Phot.* 11, 678–680 (2017).
- [3] H. Lo, M. Curty, and B. Qi. Measurement-Device-Independent Quantum Key Distribution, *Phys. Rev. Lett.* 108, 130503 (2012).
- [4] S. Lloyd, M. S. Shahriar, J. H. Shapiro, and P. R. Hemmer. Long Distance, Unconditional Teleportation of Atomic States via Complete Bell-state Measurements, *Phys. Rev. Lett.* 87, 167903 (2001).
- [5] B. Hensen, N. Kalb, M.S. Blok, A. E. Dréau, A. Reiserer, R. F. L. Vermeulen, R. N. Schouten, M. Markham, D. J. Twitchen, K. Goodenough, D. Elkouss, S. Wehner, T. H. Taminiau, and R. Hanson. Loophole-free Bell test using electron spins in diamond: second experiment and additional analysis, *Sci. Rep.* 6, 30289 (2016).
- [6] R. Valivarthi, M. G. Puigibert, Q. Zhou, G. H. Aguilar, V. B. Verma, F. Marsili, M. D. Shaw, S. W. Nam, D. Oblak, and W. Tittel. Quantum teleportation across a metropolitan fiber network, *Nat. Phot.* 10, 676–680 (2016).
- [7] Q. Sun, Y. Mao, S. Chen, W. Zhang, Y. Jiang, Y. Zhang, W. Zhang, S. Miki, T. Yamashita, H. Terai, X. Jiang, T. Chen, L. You, X. Chen, Z. Wang, J. Fan, Q. Zhang, and J.W. Pan. Quantum teleportation with independent sources and prior entanglement distribution over a network, *Nat. Phot.* 10, 671–675 (2016).
- [8] R. Valivarthi et al., Teleportation Systems Toward a Quantum Internet, *Phys. Rev. X Quantum* 1, 020317 (2020).
- [9] M. Puigibert, Entanglement and nonlocality between disparate solid-state quantum memories mediated by photons, *Phys. Rev. Research* 2, 013039 (2020).

- [10] M. Cao et al., Efficient reversible entanglement transfer between light and quantum memories, *Optica* 7, 1440 (2020).
- [11] L. Slodicka et al., Atom-Atom Entanglement by Single-Photon Detection, *Phys. Rev. Lett.* 110, 083603 (2013).
- [12] P. van Loock et al., Extending Quantum Links: Modules for Fiber- and Memory-Based Quantum Repeaters, *Adv. Quantum Technol.* 3, 1900141 (2020).
- [13] Quantum Networks for Open Science Workshop, Office of Advanced Scientific Computing Research, Department of Energy, DOI: 10.2172/1499146 (2020).
- [14] Awschalom2019 D. Awschalom, et al., Development of Quantum InterConnects (QuICs) for Next-Generation Information Technologies, *arXiv:1912.06642* (2019).
- [15] Report of the DOE Quantum Internet Blueprint Workshop, From Long-distance Entanglement to Building a Nationwide Quantum Internet (2020).
- [16] Y. Wang, J. Li, S. Zhang, K. Su, Y. Zhou, K. Liao, S. Du, H. Yan, and S. Zhu. Efficient quantum memory for single-photon polarization qubits, *Nat. Phot.* 13, 346-351, (2019).
- [17] S. Yang, X. Wang, X. Bao, and J.W. Pan. An efficient quantum light-matter interface with sub-second lifetime. *Nat. Phot.* 10, 381–384 (2016).
- [18] B. Jing, X. Wang, Y. Yu, P. F. Sun, Y. Jiang, S. J. Yang, W. H. Jiang, X. Y. Luo, J. Zhang, X. Jiang, X. H. Bao, and J. W. Pan. Entanglement of three quantum memories via interference of three single photons, *Nat. Phot.* 13, 210-213 (2019).
- [19] Y. Yu, F. Ma, X. Luo, B. Jing, P. Sun, R. Fang, C. Yang, H. Liu, M. Zheng, X. Xie, W. Zhang, L. You, Z. Wang, T. Chen, Q. Zhang, X. Bao, and J. W. Pan. *arXiv:1903.11284* (2019).
- [20] L.M. Duan, M. D. Lukin, J. I. Cirac, and P. Zoller. Long-distance quantum communication with atomic ensembles and linear optics. *Nature*, 414, 6862 (2001).
- [21] C. Cabrillo, J. Dirac, P. Fernandez, and P. Zoller. Creation of entangled states of distant atoms by interference. *Phys. Rev. A* 59, 1025–1033 (1999).
- [22] I. Novikova, R. Walsworth, and Y. Xiao. Electromagnetically induced transparency-based slow and stored light in warm atoms. *Las. Phot. Rev.* 6, 333–353 (2012).
C. Kupchak, T. Mittiga, B. Jordaan, M. Namazi, C. Nölleke, and E. Figueroa. Room-Temperature Single-photon level Memory for Polarization States, *Sci. Rep.* 5, 7658 (2015).
- [23] M. Namazi, C. Kupchak, B. Jordaan, R. Shahrokhshahi, and E. Figueroa. Ultralow-Noise Room-Temperature Quantum Memory for Polarization Qubits, *Phys. Rev. App.* 8, 034023 (2017).
- [24] R. Finkelstein, E. Poem, O. Michel, O. Lahad, and O. Firstenberg. Fast, noise-free memory for photon synchronization at room temperature. *Sci. Adv.* 4, eaap8598 (2018).
- [25] K. T. Kaczmarek, P. M. Ledingham, B. Brecht, S. E. Thomas, G. S. Thekkadath, O. Lazo-Arjona, J. H. D. Munns, E. Poem, A. Feizpour, D. J. Saunders, J. Nunn, and I. A. Walmsley. High-speed noise-free optical quantum memory. *Phys. Rev. A* 97, 042316 (2018).
- [26] O. Katz, and O. Firstenberg. Light storage for one second in room-temperature alkali vapor. *Nat. Comm.* 9, 2074 (2018).
- [27] M. Namazi, G. Vallone, B. Jordaan, C. Goham, R. Shahrokhshahi, P. Villaresi, and E. Figueroa. Free-Space Quantum Communication with a Portable Quantum Memory. *Phys. Rev. App.* 8, 064013 (2017).
- [28] M. Flament et al., Hong-Ou-Mandel interference of polarization qubits stored in independent room-temperature quantum memories, *arXiv:1808.07015v2* (2019).
- [29] A. G. Radnaev, Y.O. Dudin, R. Zhao, H. H. Jen, S. D. Jenkins, A. Kuzmich, and T. A. B. Kennedy, “A quantum memory with telecom wavelength conversion,” *Nature Physics* 6, 894 (2010).
- [30] C. K. Hong, Z. Y. Ou, and L. Mandel. Measurement of Subpicosecond Time Intervals Between Two-Photon By Interference, *Phys. Rev. Lett.* 59, 18 2044–2046 (1987).
- [31] E. Saglamyurek et al., Quantum storage of entangled telecom-wavelength photons in an erbium-doped optical fibre, *Nature Photonics* 9, 83 (2015).
- [32] J. Jin, et al., Telecom-Wavelength Atomic Quantum Memory in Optical Fiber for Heralded Polarization Qubits, *Phys. Rev. Lett.* 115, 140501 (2015).
- [33] M. Falamarzi et al., Storage and Reemission of Heralded Telecommunication-Wavelength Photons Using a Crystal Waveguide, *Phys. Rev. Applied* 11, 054056 (2019).
- [34] M. Bock et al., High-fidelity entanglement between a trapped ion and a telecom photon via quantum frequency conversion, *Nature Communications* 9, 1998 (2018).
- [35] T. van Leent et al., Long-Distance Distribution of Atom-Photon Entanglement at Telecom Wavelength, *Phys. Rev. Lett.* 124, 010510 (2020).
- [36] Y. Yu et al., Entanglement of two quantum memories via fibres over dozens of kilometres, *Nature* 578, 240 (2020).